

Glide symmetry breaking and Ising criticality in the quasi-1D magnet CoNb_2O_6

Michele Fava,¹ Radu Coldea,² and S.A. Parameswaran¹

¹*Rudolf Peierls Centre for Theoretical Physics, Clarendon Laboratory, Oxford OX1 3PU, United Kingdom*

²*Clarendon Laboratory, Parks Road, Oxford OX1 3PU, United Kingdom*

(Dated: June 27, 2022)

We construct a microscopic spin-exchange Hamiltonian for the quasi-1D Ising magnet CoNb_2O_6 that captures detailed and hitherto-unexplained aspects of its dynamic spin structure factor. We perform a symmetry analysis that recalls that an individual Ising chain in this material is buckled, with two sites in each unit cell related by a glide symmetry. Combining this with numerical simulations benchmarked against neutron scattering experiments, we argue that the single-chain Hamiltonian contains a staggered spin-exchange term. We further argue that the transverse-field-tuned quantum critical point in CoNb_2O_6 corresponds to breaking this glide symmetry, rather than an on-site Ising symmetry as previously believed. This gives a unified microscopic explanation of the dispersion of confined states in the ordered phase and ‘quasiparticle breakdown’ in the polarized phase at high transverse field.

Introduction.— Magnetic materials with a large mismatch of exchange strengths along different crystalline axes can often be understood from a one-dimensional (1D) starting point. In this paper, we focus on a celebrated example of such a quasi-1D magnet, CoNb_2O_6 , usually viewed as a system of weakly-coupled ferromagnetic Ising chains. Several theoretical predictions rooted in this perspective that leverage techniques ranging from integrability and conformal field theory (CFT) to matrix-product state numerical methods have been verified via neutron scattering experiments. Especially striking among these are studies of the transverse-field-tuned quantum critical point (QCP) [1–4], considered a canonical example of the Ising universality class. However, many detailed experimental features have resisted a fully microscopic explanation. This is particularly true away from the critical regime, where perturbations to the simplest Ising description play a significant role.

Here, we revisit the models used to describe CoNb_2O_6 , paying attention to the fact that it is only a *quasi*-1D system. We use a combination of symmetry analysis, time-dependent density-matrix renormalization group (tDMRG) simulations, and exact diagonalization studies to construct a microscopic 1D model, compute its dynamical spin structure factor (DSF), and compare against that measured by inelastic neutron scattering (INS) experiments. By exploring various symmetry-allowed exchange terms beyond the dominant Ising coupling, we find that the origin of various hitherto-unexplained features of the DSF may be traced to a *single* previously-ignored contribution: namely, a staggered nearest-neighbor exchange between y - and z -axis spin components (z is the Ising axis). Its admissibility originates in a subtle and oft-overlooked feature of CoNb_2O_6 , namely that each 1D system is really a zig-zag chain of Co^{2+} ions, so that each unit cell contains two sites. In other words, it relies on the fact that the chain is embedded in a 3D crystal, leading to distinct symmetry considerations than in pure 1D. We show that this term controls

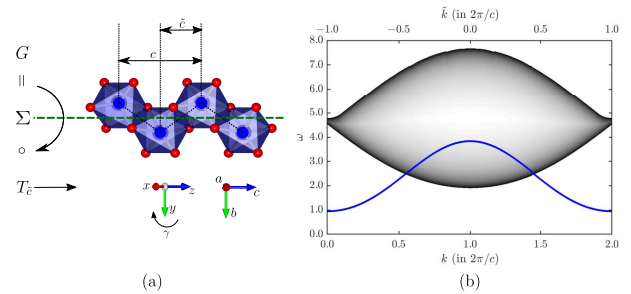


FIG. 1. (a) Individual Ising chain in CoNb_2O_6 . The zig-zag structure gives rise to a glide reflection symmetry, corresponding to an ac -plane reflection Σ followed by a half-lattice translation $T_{\bar{c}} = T_{c/2}$. (b) Excitation spectrum in the transverse-field polarized quantum paramagnetic phase, showing the band of single spin-flip QPs (blue solid line) and the 2QP continuum (shaded region; darker shading indicates higher density of states). The x -axis shows both momentum k (bottom) and glide eigenvalue \tilde{k} (top). The position of the 2QP continuum relative to the 1QP band is controlled by conservation of \tilde{k} , rather than k , as detailed in the text.

both (i) the dispersion of confined bound states of two domain wall (DW) excitations [5–7] in the spontaneously ordered phase for zero and weak transverse fields, previously only captured phenomenologically; and (ii) quasiparticle (QP) breakdown, a phenomenon observed [8] in the opposite limit when a strong transverse field drives the system into a polarized quantum paramagnet.

The staggered coupling we consider explicitly breaks both Ising and translational symmetry. Nevertheless, we show that it may be reconciled both with the host of results predicated on the existence of an Ising QCP in CoNb_2O_6 and with the absence of Brillouin zone (BZ) halving in the DSF throughout the field-polarized phase. This is because the chain retains a glide symmetry composed of translation by half a lattice spacing ($\bar{c} = c/2$ in

Fig 1(a)) combined with a reflection; the ordered phase breaks this symmetry. A unitary transformation maps the symmetries of our model to those of an Ising *antiferromagnet* in a transverse field, and the glide-breaking transition to the breaking of discrete translational symmetry in that model, known to be in the Ising universality class [9–11]. The transformed Hamiltonian has a single-site unit cell, and the transformation effectively “unfolds” the BZ probed by DSF into one twice as large (size $4\pi/c$) — i.e., the same as that observed in experiments. Unit cell doubling is manifest in the DSF only upon *breaking* the glide symmetry, allowing scattering to directly probe the glide-breaking order parameter. We show that glide symmetry provides a natural kinematic interpretation of quasiparticle breakdown in the high-field-polarized phase: the decay processes that drive it are constrained by glide selection rules rather than by momentum conservation. This scenario provides a natural explanation of several important features of experimental INS data. Our work gives a fully microscopic understanding of Ising criticality, confinement, and QP breakdown in CoNb_2O_6 , providing a platform for further studies, and illustrates the subtle interplay of spatial and on-site symmetries in chain- and layer- compounds with non-symmorphic space groups.

Symmetries and Microscopic Hamiltonian.— In CoNb_2O_6 , Co^{2+} ions hosting pseudospin-1/2 moments are arranged in zig-zag chains along the c -axis, with a dominant ferromagnetic Ising coupling along the chain. The chains form a triangular lattice in the ab plane, with nearest-neighbor chains weakly coupled antiferromagnetically. The 3D space group is $Pbcn$ (No. 60), which includes a glide plane that intersects each chain perpendicular to its zig-zag plane [ac -plane in Fig. 1(a)]. Henceforth we focus on a single chain, and denote by S_j^α the α -component of the spin operator acting on the j -th site (even and odd sites lie on different sublattices), with $\alpha \in \{x, y, z\}$, defined as in Fig. 1(a). The Ising axis z lies in the ac -plane at an angle $\gamma = 29.6^\circ$ to c [12], while b is parallel to y . Recalling the two-site unit cell, the simplest nearest-neighbor exchange Hamiltonian takes the form

$$\mathcal{H}_{\text{nn}} = \sum_j \sum_{\alpha, \beta} \mathcal{J}_{\alpha, \beta}^{(1)} S_{2j}^\alpha S_{2j+1}^\beta + \mathcal{J}_{\alpha, \beta}^{(2)} S_{2j+1}^\alpha S_{2j+2}^\beta. \quad (1)$$

Crystal symmetry further constrains $\mathcal{J}_{\alpha, \beta}^{(n)}$. Inversion about the mid-point between consecutive spins requires $\mathcal{J}_{\alpha, \beta}^{(n)} = \mathcal{J}_{\beta, \alpha}^{(n)}$, while the glide symmetry imposes

$$\mathcal{J}_{\alpha, \beta}^{(1)} = \begin{cases} -\mathcal{J}_{\alpha, \beta}^{(2)} & \text{if } \beta = y \neq \alpha, \\ \mathcal{J}_{\alpha, \beta}^{(2)} & \text{otherwise.} \end{cases} \quad (2)$$

The most general exchange tensor satisfying these conditions may be parametrized (in the xyz basis) as

$$\mathcal{J}^{(m)} = J \begin{pmatrix} \lambda_S + \lambda_A & (-1)^m \lambda_{xy} & \lambda_{xz} \\ (-1)^m \lambda_{xy} & \lambda_S - \lambda_A & (-1)^m \lambda_{yz} \\ \lambda_{xz} & (-1)^m \lambda_{yz} & -1 \end{pmatrix} \quad (3)$$

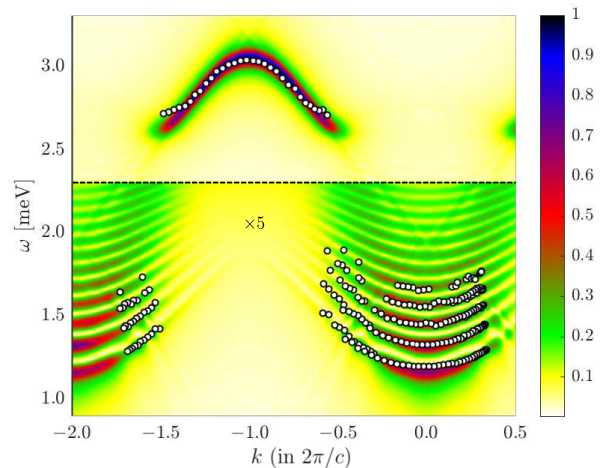


FIG. 2. DSF $\mathcal{S}^{xx}(\omega, k)$ at $h_y = 0$, scaled by a factor of 5 below the dashed line. Dots denote dispersion data points from the INS data of Ref. 5. (tDMRG simulations truncated singular values $\lesssim \varepsilon = 2 \cdot 10^{-11}$ and used a Trotter step $\delta t = 2.5 \cdot 10^{-3}/J$ and broadening $\eta = J/125$ [13].)

with $m = 1, 2$ and $J > 0$. Taking z along the Ising axis sets $\lambda_{xz} = 0$. Since the nearest-neighbour ferromagnetic coupling J dominates, we anticipate all $\lambda \lesssim 1$.

Neutron scattering probes the DSF, which is related to the spin-spin correlation function of Hamiltonian \mathcal{H} via

$$\mathcal{S}^{\alpha\beta}(\omega, k) \equiv \frac{1}{L} \int_{-\infty}^{\infty} dt \sum_{i,j} e^{ik(r_i - r_j)} e^{i\omega t} \langle S_i^\alpha(t) S_j^\beta \rangle, \quad (4)$$

where $S_j^\alpha(t) = e^{i\mathcal{H}t} S_j^\alpha e^{-i\mathcal{H}t}$ and L is the total number of sites. For transverse (b -axis) field $h_y = 0$, operators $S_j^{x,y}$ excite a pair of DW excitations of the (Ising) ordered state. These are confined by a longitudinal (z -axis) mean field h_z . We constrain allowed terms in \mathcal{H} by requiring that it reproduces perturbatively to $O(\lambda/J)$ the effective Hamiltonian for DW motion from [5, 6]. This yields

$$\mathcal{H} = J \sum_j \left[-S_j^z S_{j+1}^z + \lambda_{\text{AF}} S_j^z S_{j+2}^z + h_y S_j^y + \lambda_S (S_j^x S_{j+1}^x + S_j^y S_{j+1}^y) - h_z S_j^z \right] + \mathcal{H}_{dw}, \quad (5)$$

which includes a next-nearest neighbor antiferromagnetic λ_{AF} term [6, 8] as well as an effective longitudinal field $h_z = J_{\text{ic}}^{zz} \sum_j \langle S_j^z \rangle / L$ accounting for interchain coupling (parameterized by J_{ic}^{zz}) at the mean-field level. Both of these (as well as λ_S) are needed to reproduce details of the experimental zero-field DSF [5]. We also include a transverse field $h_y = g_b \mu_B B$, where B is an external magnetic field. The final term \mathcal{H}_{dw} in (5) gives dynamics to DWs; since its magnitude [5, 6] is much larger than that of inter-chain couplings (which are $\sim h_z$ [14]), it cannot arise primarily from these. A key goal of this work is to identify a microscopic origin for this DW hopping, that was previously only modeled phenomenologically [6]. Accordingly, we first note that the only symmetry-allowed

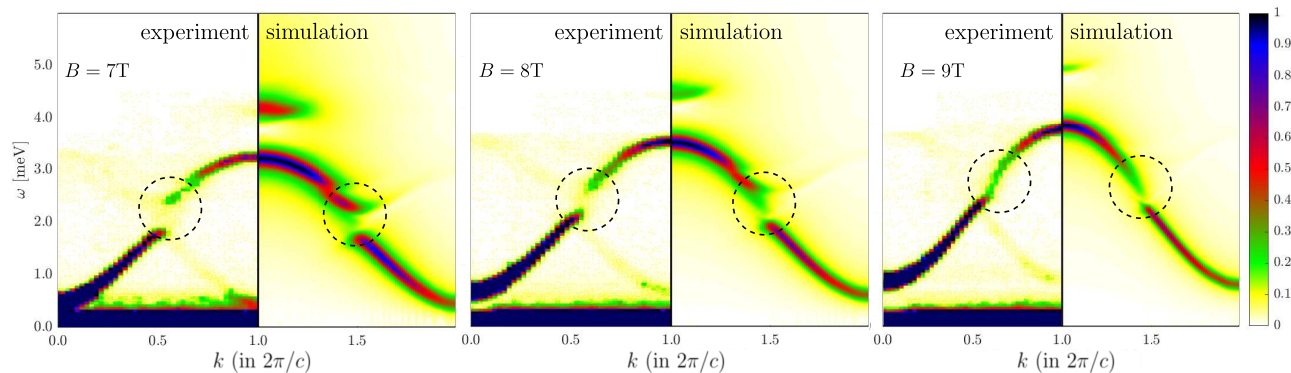


FIG. 3. Evolution of DSF in the polarized phase at large transverse field, comparing experimental data from Ref. [8] (left) to tDMRG simulations of $S^{xx}(\omega, k)$ for the 1D Hamiltonian (5) (right). Dashed circles indicate the regions of QP breakdown. (tDMRG parameters: $\delta t = 5 \cdot 10^{-3}/J$, $\varepsilon = 2 \cdot 10^{-10}$, $\chi_{max} = 400$, $\eta = J/60$ [13]).

nearest-neighbour exchange couplings yielding DW hopping are those denoted λ_A , λ_{xy} and λ_{yz} in (3). Of these, λ_A , λ_{xy} yield a DSF with doubled k -space periodicity relative to experiments [13]. Thus, we take

$$\mathcal{H}_{dw} = J \sum_j \lambda_{yz} (-1)^j (S_j^z S_{j+1}^y + S_j^y S_{j+1}^z). \quad (6)$$

While $\mathcal{H} - \mathcal{H}_{dw}$ is symmetric under translation $T_{\tilde{c}} : r_j \mapsto r_j + \tilde{c}$ by a nearest-neighbor spacing \tilde{c} , \mathcal{H}_{dw} only preserves translation T_c , with $c = 2\tilde{c}$. However, this unit cell doubling is invisible in the DSF which is consistent with a BZ of size $2\pi/\tilde{c}$ (see Fig. 2). Below, we link this to a non-symmorphic glide symmetry $G \equiv T_{\tilde{c}} \circ \Sigma$, i.e. a translation by half a unit cell composed with a spin-flip $\Sigma = e^{i\pi \sum_j S_j^y}$ in the ab plane (consistent with the spatial reflection of a pseudovector spin). First, however, we determine the magnitude of the couplings in \mathcal{H} .

Numerical results. — We fix the parameters in \mathcal{H} using exact diagonalization on small system sizes with $h_y = 0$. Through the fitting procedure described in the supplement [13], we find $J = 2.7607$ meV, $\lambda_{AF} = 0.1507$, $\lambda_S = 0.2392$, $\lambda_{yz} = 0.1647$, and $J_{ic}^{zz} = 0.0312$ meV. For the Hamiltonian thus obtained we compute the DSF for an effectively infinite system using tDMRG [13]. Our numerical results match the experimental data well (Fig. 2). We also compute the DSF in the high-field quantum paramagnetic regime, achieved for sufficiently strong transverse (i.e., b -axis) field. We set $h_z = 0$, consistent with the fact that the inter-chain mean field vanishes when $\langle S_j^z \rangle = 0$. To match simulations with data, we estimated $g_b \simeq 3.100$ by fitting the experimental dispersion at $B = 7T$ [13]. A direct comparison of our results against data from [8] (Fig. 3) shows excellent agreement, including features associated with “quasiparticle breakdown” — i.e., the apparent break in the dispersion of the QP band, traditionally understood as a decay of a QP as it enters the two-QP continuum, that occurs for sufficiently strong coupling (see, e.g. [8]). We now rationalize these results in terms of symmetries of \mathcal{H} .

Ising criticality, glide symmetry, and BZ unfolding. — Hamiltonian (5) has neither translational symmetry by a nearest-neighbor spacing ($T_{\tilde{c}}$) nor on-site Ising symmetry (generated by Σ) as neither commutes with \mathcal{H}_{dw} . However, it preserves their product: glide symmetry G .

We now consider the unitary transformation $U = U^{-1} = e^{i\pi \sum_j S_j^y}$ which reverses the Ising axis on alternate sites of the chain. It is straightforward to see that the invariance of $\tilde{\mathcal{H}} = U\mathcal{H}U^{-1}$ under $T_{\tilde{c}}$ is equivalent to that of \mathcal{H} under G . The transformation flips the sign of the nearest-neighbor zz and xx couplings and staggers the h_z term, while leaving the h_y term unchanged. Crucially $\tilde{\mathcal{H}}_{dw}$ is no longer staggered, and hence preserves $T_{\tilde{c}}$, but continues to break global Ising symmetry $S_j^z \mapsto -S_j^z$. Thus, $\tilde{\mathcal{H}}$ describes a translationally-invariant Ising antiferromagnet (AF) in a uniform transverse field h_y , with additional terms that break global Ising symmetry, augmented with a field h_z that couples to the AF order parameter field $m_s = \sum_j (-1)^j \langle S_j^z \rangle / L$. For $h_z = 0$, $\tilde{\mathcal{H}}$ continues to have a transition in the Ising universality class, since the AF order parameter spontaneously breaks the lattice symmetry [9, 10] (see also [11]). Reversing the unitary transformation, we see that this corresponds to the spontaneous breaking of the glide symmetry of \mathcal{H} . In the ordered phase $h_z \neq 0$ due to the inter-chain mean field, and couples to the order parameter field m_s . Therefore, the near-critical ordered phase is described by the Ising CFT perturbed by the magnetization operator — precisely that for which E_8 -symmetry-related bound states were predicted [15] and experimentally identified [5]. Therefore, although our revised model (5) associates the Ising criticality of CoNb_2O_6 with the spontaneous breaking of glide symmetry rather than the on-site Ising symmetry, it remains consistent with previously-reported experiments.

The unitary transformation also allows us to view scattering experiments as probing the DSF of $\tilde{\mathcal{H}}$ (up to a k -space shift). To see this, observe that the DSF of

$S_k^\mu = \sum_j e^{ikj\tilde{c}} S_j^\mu$ under the dynamics generated by \mathcal{H} is equal to the DSF of $\tilde{S}_k^\mu = U S_k^\mu U^{-1}$ under the dynamics generated by $\tilde{\mathcal{H}}$, as can be seen by inserting $U^{-1}U = \mathbf{1}$ in (4). Either by studying the commutation relations of \tilde{S}_k^μ with $T_{\tilde{c}}$ or directly by inspecting $\tilde{S}_k^\mu = \sum_j e^{ikj\tilde{c}} U S_j^\mu U^{-1}$, we see that S_k^μ changes the momentum as $\tilde{k} = k + \delta_\mu$ where $\delta_{x,z} = \pi/\tilde{c}$, and $\delta_y = 0$. Consequently, since $\tilde{\mathcal{H}}$ has a unit cell of length \tilde{c} , the DSF will be $2\pi/\tilde{c}$ -periodic as long as G is unbroken (i.e. in the high-field paramagnetic phase). In the ordered phase, where G is broken, we expect that the DSF is only $2\pi/c$ -periodic (i.e. sees a smaller BZ). This is also corroborated by INS data Fig. 4. Note however that exactly at $h_y = 0$ we recover $2\pi/\tilde{c}$ -periodicity of the DSF as evident in Fig. 2, since \mathcal{H} has an extra glide symmetry given by $G' = T_{\tilde{c}} \circ e^{i\pi \sum_j S_j^z}$, which is explicitly broken for $h_y \neq 0$. [The same conclusions follow from the commutators of G with S_k^μ , as the operators G and $T_{\tilde{c}}$ are related by the unfolding U [13].]

We now use this BZ unfolding perspective to interpret experiments on CoNb_2O_6 . Scattering non-polarized neutrons from a sample should yield superposition of the DSF of \tilde{H} (from the y component) and the same DSF shifted in momentum k by π/\tilde{c} (from the x and z components). However in the high-field polarized phase $\langle S_j^y \rangle$ is near saturation, thus largely suppressing the inelastic b component of the DSF. Hence, the dominant signal observed in this phase is the one at $k = \tilde{k} + \pi/\tilde{c}$; shifting the glide-labeled spectrum by π/\tilde{c} thus reproduces the measurements. [A weaker-intensity “shadow mode” shifted by π/\tilde{c} visible in the experimental data is due to a weak explicit breaking of glide symmetry by components of the scattering wavevector transverse to the chain [13, 14].]

Quasiparticle breakdown.— The elementary excitations of the high-field phase are dressed spin-flips relative to the b -axis field. For $\lambda \neq 0$, these are interacting quasiparticles with rich physics. As seen in experiments and reproduced by our model (Fig. 3), they exhibit the striking feature of quasiparticle breakdown. Glide symmetry provides a natural resolution of why the decay of a single QP into the 2-QP continuum that causes this effect is limited to a narrow, field-dependent range of momenta, (Fig. 3). First, matching the k values with their respective \tilde{k} as described above, we find that the minimum (maximum) of the single-QP dispersion $\omega_{\text{QP}}(\tilde{k})$ is at $\tilde{k} = \pi/\tilde{c}$ ($\tilde{k} = 0$) as shown in Fig. 1. We stress that only \tilde{k} is a good quantum number for \mathcal{H} , rather than the experimental wavevector k . With this in mind, the states that form part of the two-QP continuum in the (\tilde{k}, ω) plane are those satisfying $\tilde{k} = \tilde{k}_1 + \tilde{k}_2$, $\omega = \omega_{\text{QP}}(\tilde{k}_1) + \omega_{\text{QP}}(\tilde{k}_2)$. From this, we see that the entire upper section of the single-QP band is immersed in the continuum (Fig. 1(b)). We emphasize that this is sharply distinct [13] from approaches that do not incorporate the glide symmetry and the corresponding π/\tilde{c} momentum shifts (compare Fig. 1(b) to Figs. 2, 6 of [8]).

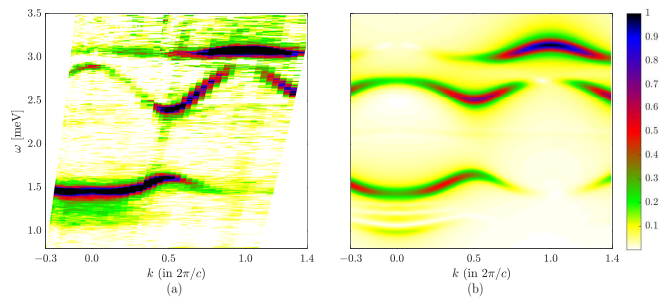


FIG. 4. (a) DSF measured by INS experiments in the ordered phase at intermediate transverse field (2.5 T) [16]. Sharp modes show the reduced periodicity of the structural $2\pi/c$ BZ, in contrast to the $4\pi/c$ periodicity in the ordered phase at zero field (Fig. 2) and the high-field paramagnetic phase (Fig. 3). This is tied to the breaking of glide symmetry G throughout the ordered phase except at $h_y = 0$, which enjoys an extra glide symmetry G' . (b) DSF $S^{xx}(k, \omega)$ calculated via tDMRG ($\delta t = 2.5 \cdot 10^{-3}/J$, $\varepsilon = 2 \cdot 10^{-11}$, $\eta = J/100$ [13]). Key features of the spectrum in (a) including all dispersion shapes are qualitatively well-reproduced, justifying the minimal Hamiltonian (5). More precise quantitative agreement requires fitting data to the tDMRG simulations of (5) rather than a perturbative low-energy model [13]. This is very computationally demanding and beyond the scope of this work.

Now, the QP-continuum matrix elements are at most $O(\lambda_{yz})$, as for $\lambda_{yz} = 0$ the decay would be forbidden by \mathbb{Z}_2 (Ising) symmetry. Using Fermi’s Golden rule and neglecting to first approximation the dependence of matrix elements on momenta, the QP decay rate at wave vector k may be estimated as $\Gamma(k) \sim |\lambda_{yz}|^2 \rho_2(\tilde{k}, \omega(\tilde{k}))$. Here $\rho_2(\tilde{k}, \omega)$ is the two-QP density of states (DoS), which has a $(\omega - \omega_c(k))^{-1/2}$ singularity near the edges of the 2QP continuum [17–19]. Hence, although in much of the 2QP continuum the decay rate is suppressed by $|\lambda_{yz}|^2 \ll 1$, the DoS singularity near its edge will produce full QP breakdown. This explains the relatively narrow region in momentum space where breakdown is visible in Fig. 3.

Discussion.— We have constructed a microscopic spin-exchange Hamiltonian to describe the 1D physics of CoNb_2O_6 , based on a symmetry analysis of its 3D space group. We found quantitative agreement between simulations of the model and INS experiments in very different regimes, indicating that the proposed model realistically captures single-chain physics.

A crucial departure from previous studies lies in the symmetries of our model, which identifies a two-site unit cell and explicitly breaks the on-site Ising \mathbb{Z}_2 symmetry. However, it retains a glide symmetry inherited from the 3D space group. We showed through an explicit unfolding transformation that the glide symmetry leads to a larger BZ for INS than that expected from the size of the unit cell. This transformation also shows that the model is consistent with previous reports of Ising criticality in CoNb_2O_6 , if the ordering is linked to the breaking of glide symmetry rather than on-site \mathbb{Z}_2 .

Our work reveals how subtle aspects of crystal symmetry intertwine with the rich physics of quantum criticality, and provides a unified picture of spontaneous ordering, confinement, and quasiparticle breakdown in a canonical Ising-chain system. It raises further interesting questions as to how symmetry considerations impact the rich 3D phase structure of CoNb_2O_6 . Similar ideas are likely relevant to other chain and layer compounds with non-symmorphic space groups [13].

Acknowledgements.— We thank Sarang Gopalakrishnan, Fabian Essler, and John Chalker for useful discussions. We acknowledge support from the the European Research Council under the European Union Horizon 2020 Research and Innovation Programme via Grant Agreements No. 788814-EQFT (RC) and 804213-TMCS (SAP). Numerical simulations were performed using the ITensor Library [20].

-
- [1] C. M. Morris, R. Valdés Aguilar, A. Ghosh, S. M. Koohpayeh, J. Krizan, R. J. Cava, O. Tchernyshyov, T. M. McQueen, and N. P. Armitage, *Phys. Rev. Lett.* **112**, 137403 (2014).
- [2] A. W. Kinross, M. Fu, T. J. Munsie, H. A. Dabkowska, G. M. Luke, S. Sachdev, and T. Imai, *Phys. Rev. X* **4**, 031008 (2014).
- [3] T. Liang, S. Koohpayeh, J. Krizan, T. McQueen, R. J. Cava, and N. P. Ong, *Nature communications* **6**, 7611 (2015).
- [4] C. T. Bach, N. T. Nguyen, and G. H. Bach, *Journal of Magnetism and Magnetic Materials* **483**, 136 (2019).
- [5] R. Coldea, D. A. Tennant, E. M. Wheeler, E. Wawrzynska, D. Prabhakaran, M. Telling, K. Habicht, P. Smeibidl, and K. Kiefer, *Science* **327**, 177 (2010).
- [6] J. A. Kjäll, F. Pollmann, and J. E. Moore, *Phys. Rev. B* **83**, 020407 (2011).
- [7] S. B. Rutkevich, *Journal of Statistical Mechanics: Theory and Experiment* **2010**, P07015 (2010).
- [8] N. J. Robinson, F. H. L. Essler, I. Cabrera, and R. Coldea, *Phys. Rev. B* **90**, 174406 (2014).
- [9] S. Sachdev, K. Sengupta, and S. M. Girvin, *Phys. Rev. B* **66**, 075128 (2002).
- [10] A. A. Ovchinnikov, D. V. Dmitriev, V. Y. Krivnov, and V. O. Chervanovskii, *Phys. Rev. B* **68**, 214406 (2003).
- [11] M. A. Neto and J. R. de Sousa, *Physica A: Statistical Mechanics and its Applications* **392**, 1 (2013).
- [12] C. Heid, H. Weitzel, P. Burlet, M. Bonnet, W. Gonschorek, T. Vogt, J. Norwig, and H. Fuess, *Journal of Magnetism and Magnetic Materials* **151**, 123 (1995).
- [13] See Supplemental Material associated with this manuscript.
- [14] I. Cabrera, J. D. Thompson, R. Coldea, D. Prabhakaran, R. I. Bewley, T. Guidi, J. A. Rodriguez-Rivera, and C. Stock, *Phys. Rev. B* **90**, 014418 (2014).
- [15] A. B. Zamolodchikov, *International Journal of Modern Physics A* **04**, 4235 (1989), <https://doi.org/10.1142/S0217751X8900176X>.
- [16] R. Coldea *et al.*, (2020), in preparation.
- [17] B. Gaveau and L. S. Schulman, *Journal of Physics A: Mathematical and General* **28**, 7359 (1995).
- [18] M. E. Zhitomirsky and A. L. Chernyshev, *Rev. Mod. Phys.* **85**, 219 (2013).
- [19] R. Verresen, R. Moessner, and F. Pollmann, *Nature Physics* **15**, 750 (2019).
- [20] ITensor Library (version 2.0.11) <http://itensor.org>.
- [21] S. A. Parameswaran, *Journal of Physics: Condensed Matter* **31**, 104001 (2019).
- [22] S. Paeckel, T. Köhler, A. Swoboda, S. R. Manmana, U. Schollwöck, and C. Hubig, *Annals Phys.* **411**, 167998 (2019), [arXiv:1901.05824 \[cond-mat.str-el\]](https://arxiv.org/abs/1901.05824).
- [23] S. R. White and I. Affleck, *Phys. Rev. B* **77**, 134437 (2008).

**SUPPLEMENTARY INFORMATION FOR “GLIDE SYMMETRY BREAKING AND ISING
CRITICALITY IN THE QUASI-1D MAGNET CONB₂O₆”**

Dispersion of the 2-DW spectra in perturbation theory for different terms

In this appendix we derive an effective Hamiltonian for \mathcal{H} with the addition of other symmetry allowed terms in zero external magnetic field $h_y = 0$. To do so, we treat perturbatively all the couplings w.r.t. the ferromagnetic one. We expect this approach to give qualitatively correct results, since all couplings λ are at most of order 10^{-1} . In particular, we consider (one at a time) the effect of a non-zero λ_{xy} , λ_{yz} and λ_A (on top of the other terms in \mathcal{H} (5)).

$\mathcal{H}_f = -J \sum_j S_j^z S_{j+1}^z$ splits the Hilbert space in highly degenerate multiplets, the energy of which is set by the number of domain walls. At first order in perturbation theory, we neglect the mixing between different multiplets and project the couplings of the Hamiltonian into a given multiplet. Since we are interested in eigenstates that are connected to the ground states through a single spin-flip, as these are the ones giving a dominant contribution to the DSF, we focus on the multiplet with 2 domain-walls.

A complete basis in this multiplet is given by

$$|j, l\rangle := |\cdots \uparrow \underbrace{\uparrow \downarrow}_j \underbrace{\downarrow \uparrow}_{j+1} \cdots \downarrow \underbrace{\downarrow \uparrow}_{j+l} \underbrace{\uparrow \downarrow}_{j+l+1} \cdots\rangle \quad (\text{S1})$$

Denoting the ground state energy of \mathcal{H} (at first order in perturbation theory) with E_0 , and defining $|j, l \leq 0\rangle \equiv 0$, we have

$$\frac{H - E_0}{J} |j, l\rangle = (1 - 2\lambda_{\text{AF}} + h_z l + \delta_{l,1} \lambda_{\text{AF}}) |j, l\rangle - \frac{\lambda_S}{2} \delta_{l,1} (|j+1, 1\rangle + |j-1, 1\rangle) + T |j, l\rangle \quad (\text{S2})$$

with T , depending on the terms added to \mathcal{H} , being

$$J\lambda_A \sum_j (S_i^x S_{j+1}^x - S_j^y S_{j+1}^y):$$

$$T_1 |j, l\rangle = \frac{\lambda_A}{2} (|j+2, l-2\rangle + |j-2, l+2\rangle + |j, l+2\rangle + |j, l-2\rangle) \quad (\text{S3})$$

$$J\lambda_{xy} \sum_j (-1)^j (S_i^x S_{i+1}^y + S_i^y S_{i+1}^x):$$

$$T_2 |j, l\rangle = \frac{\lambda_{xy} i}{2} [(-1)^j (|j+2, l-2\rangle - |j-2, l+2\rangle) - (-1)^{j+l} (|j, l+2\rangle - |j, l-2\rangle)] \quad (\text{S4})$$

$$J\lambda_{yz} \sum_j (-1)^j (S_i^y S_{i+1}^z + S_i^z S_{i+1}^y):$$

$$T_3 |j, l\rangle = \frac{\lambda_{yz} i}{2} [(-1)^j (|j+1, l-1\rangle + |j-1, l+1\rangle) + (-1)^{j+l} (|j, l+1\rangle + |j, l-1\rangle)] \quad (\text{S5})$$

The shape of the DW continuum is set by the form of T , while the other couplings result in an effective nearest-neighbour interaction between a pair of DWs.

To understand the shape of the continuum for the different terms, we move to the momentum eigensates: (setting $\tilde{c} = 1$)

$$|k, l\rangle = \frac{1}{\sqrt{L}} \sum_j e^{ikj} |j, l\rangle \quad (\text{S6})$$

Rewriting the T matrix elements in this basis, we obtain respectively

$$T_1 |k, l\rangle = \frac{\lambda_A}{2} [(e^{-2ik} + 1) |k, l-2\rangle + (e^{2ik} + 1) |k, l+2\rangle] \quad (\text{S7})$$

$$T_2 |k, l\rangle = \frac{\lambda_{xy} i}{2} [(e^{-2ik} + e^{i\pi l}) |k + \pi, l-2\rangle - (e^{2ik} + e^{i\pi l}) |k + \pi, l+2\rangle] \quad (\text{S8})$$

$$T_3 |k, l\rangle = \frac{\lambda_{yz} i}{2} [(e^{-ik} + e^{i\pi l}) |k + \pi, l - 1\rangle + (e^{ik} + e^{i\pi l}) |k + \pi, l + 1\rangle] \quad (\text{S9})$$

The presence of a term e^{2ik} in T_1 and T_2 would produce a DW continuum with periodicity π/\tilde{c} , i.e. half the periodicity observed experimentally. Instead the last term correctly produces a continuum with periodicity $2\pi/\tilde{c}$. Henceforth it is reasonable that λ_A and λ_{xy} are negligible w.r.t. λ_{yz} .

Note that the mixing between the k and $k + \pi$ sector is not enough to produce a Brillouin halving visible through the DSF. In fact, that would require the states $|k, l = 1\rangle$ and $|k + \pi, l = 1\rangle$ to belong to the same connected component of the Hilbert space, i.e. $|k + \pi, l = 1\rangle$ can be obtained by applying the Hamiltonian on $|k, l = 1\rangle$ some arbitrary number of times.

Fit of parameters for $h_y = 0$

In order to fix the 5 parameters (J , λ_{AF} , λ_S , λ_{yz} and J_{ic}^{zz}) of the Hamiltonian for $h_y = 0$, we resort to exact diagonalization on a small system of size $L = 14$. We checked that the dispersions of the 2 lowest confined bound states, unlike those of higher ones, are not strongly affected by finite size effects at $L = 14$. Furthermore, their dispersion can be quickly accessed by targeting the low-energy subspace using the Lanczos algorithm. We thus fitted parameters to minimize the square difference of the energy dispersion as obtained in two different ways: (i) experimentally, from INS [5] and (ii) numerically, by interpolating exact-diagonalization results on an $L = 14$ site system, restricting our attention to the lowest two modes.

In order to avoid overfitting, we constrained the parameters to reproduce (at first order in perturbation theory) the dispersion of the kinetic mode as parametrized in Ref. 5. This fixes

$$J\lambda_S = 0.6605 \text{ meV} \quad (\text{S10})$$

$$(1 - \lambda_{AF})J = 2.3447 \text{ meV} \quad (\text{S11})$$

thus leaving only three free parameters to be fitted.

Glide-symmetry counting

In this section we work directly with the Hamiltonian \mathcal{H} and re-derive the same results presented in the main text using the unfolding unitary transformation. Specifically, we rederive the enlarged BZ size probed by the DSF and the argument for QP breakdown (in the next section).

Before diving into the derivation note that, in general, the origin of the correspondence between the two approaches lies in the following. A given eigenstate of \mathcal{H} $|n\rangle$ will be an eigenstate of G , viz. $G|n\rangle = e^{i\varphi}|n\rangle$. As $G = T_{\tilde{c}}(T_{\tilde{c}}^\dagger U T_{\tilde{c}})U = U T_{\tilde{c}} U$, the corresponding eigenstate $|\tilde{n}\rangle = U|n\rangle$ of \tilde{H} , satisfies $T_{\tilde{c}}|\tilde{n}\rangle = e^{i\varphi}|\tilde{n}\rangle$. Therefore the glide eigenvalue is $e^{i\varphi}$ with $\varphi = \tilde{k}\tilde{c}$, where we use the same notation for the eigenvalues $e^{i\tilde{k}\tilde{c}}$ of $T_{\tilde{c}}$ as in the main text.

We now turn to the derivation, First, we re-express the DSF as

$$S^{\alpha,\beta}(\omega, k) = \sum_{n \neq m} \langle m | S^\alpha(-k) | n \rangle \langle n | S^\beta(k) | m \rangle \delta(\omega_n - \omega_m - \omega) P_m, \quad (\text{S12})$$

where ω_n is the energy of $|n\rangle$ and $P_m \propto e^{-\omega_m/T}$ is the thermal probability (Boltzmann weight) associated to the eigenstate $|m\rangle$.

In order to understand which $|n\rangle$ contributes to this sum, i.e. yield $\langle n | S^\beta(k) | 0 \rangle, \langle n | S^\alpha(k) | 0 \rangle \neq 0$, we insert the identity $G^\dagger G = \mathbb{1}$, obtaining

$$\langle n | S^\beta(k) | m \rangle = \langle n | S^\beta(k) | m \rangle \exp[i(\varphi_m + k\tilde{c} + \delta_\beta - \varphi_n)] \quad (\text{S13})$$

and similarly for $\langle n | S^\alpha(k) | m \rangle$. Requiring these to be non-zero yields

$$\varphi_n - \varphi_m = k\tilde{c} + \delta_\alpha \pmod{2\pi}, \quad \delta_\alpha = \delta_\beta. \quad (\text{S14})$$

In this way, $S^{\alpha,\beta}(\omega, k)$ will probe the transitions with $\Delta\varphi = k\tilde{c} + \delta_\alpha \pmod{2\pi}$, hence to probe the same transition at two different k , it has to be $\Delta k = 2\pi/\tilde{c}$, i.e. the periodicity of the DSF will generally be $2\pi/\tilde{c}$, in agreement with the main text.

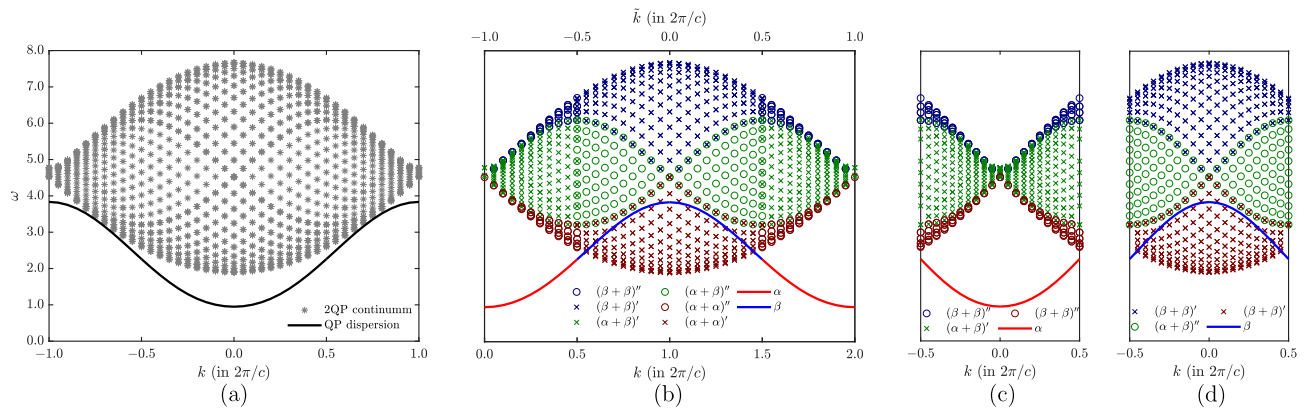


FIG. S1. (a) Single-quasiparticle dispersion $\omega_{\text{QP}}(k)$ (solid line) and the derived 2QP-continuum at $B = 9$ T, as interpolated from INS data [14]. Ignoring the the staggered term in \mathcal{H} , the 2QP continuum would be in the region denoted by grey asterisks. (b) The continuum in the (\tilde{k}, ω) plane computed taking into account the glide symmetry. (c-d) Energy dispersion in the “proper” BZ of the material (i.e. going from $k = -\pi/(2\tilde{c})$ to $k = \pi/(2\tilde{c})$). In this setting we distinguish two QP bands: α and β (red and blue curves), crossing linearly at $k = \pi/(2\tilde{c})$. They give rise to different continua distinguished by (i) the 2 QP species ($\alpha + \alpha$ in red, $\alpha + \beta$ in green, and $\beta + \beta$ in blue) or second (o) BZ. For clarity, we separated into two sub-panels the 3 continua which can couple to the α band (c) and the 3 which can couple to the β band (d). Note that only the β quasiparticles can kinematically decay.

Comparison of different ways of constructing 2QP continuum

In this section we stress the differences in the position of the 2QP continuum obtained in two ways: (i) by *incorrectly* counting momentum while ignoring the presence of a staggered term and (ii) *correctly*, by counting glide-symmetry eigenvalues.

In the first case, the 1QP band $\omega(k)$ can be obtained “as is” from the DSF. 2QP continuum states are then states with two such excitations at momenta k_1 and k_2 . In this way the quantum number of the 2QP state is $k = k_1 + k_2$, $\omega = \omega(k_1) + \omega(k_2)$. The result obtained in this way will resemble those shown in Fig. S1(a).

Instead, in the second case, we first recognize that the dominant components of the DSF observed in INS are aa and cc . Then the 1QP dispersion in the glide eigenvalue (\tilde{k}) is obtained by shifting the $\omega(k)$ band in the DSF by $k \mapsto \tilde{k} = k + \pi/\tilde{c}$ as in Fig. S1(a). A 2QP state is one formed by two QP with glide-number \tilde{k}_1 and \tilde{k}_2 . Neglecting interactions between the individual QPs, this 2QP state has energy $\omega(\tilde{k}_1, \tilde{k}_2) = \omega(\tilde{k}_1) + \omega(\tilde{k}_2)$, and glide eigenvalue $\tilde{k}(\tilde{k}_1, \tilde{k}_2) = \tilde{k}_1 + \tilde{k}_2$. This last relationship can be most conveniently obtained by performing the U transformation, exploiting the additivity of momentum and, finally, transforming back with U . The position of the continuum will be qualitatively similar to Fig. S1(b).

Finally, we outline an equivalent way of describing the QP breakdown in the glide-invariant system. If we were to ignore the glide symmetry, we would employ a BZ of full length π/\tilde{c} . The QP dispersion in the halved BZ is obtained by folding the QP dispersion as seen e.g. by INS. Due to the folding, in the smaller BZ there will appear to be 2 separate bands, which we denote by α and β (Fig. S1(c)). At $k = \pi/(2\tilde{c})$ the two bands cross linearly. While linear crossings are generally unstable in 1D, this linear crossing is protected by glide symmetry (for an example where this is worked out explicitly see Ref. 21). Since there are two bands, we can construct 3 different continua depending on the species of the two QP: $\alpha + \alpha$, $\alpha + \beta$, $\beta + \beta$. Furthermore, for each pair of QP species, we need to distinguish two sub-cases, depending on whether the sum of the two QP momenta lies in the first or second BZ, which we denote by $(\dots)'$ and $(\dots)''$ respectively. In this picture, the decay of a QP into the 2-QP continua is not only constrained by k , but also by the glide eigenvalue (Note that this step is unnecessary if one directly considers \tilde{k} , which is in 1-to-1 correspondence with the glide eigenvalues). Imposing the glide eigenvalue constraints, we find that symmetry-allowed decay channels are as follows (see also Fig. S1(c))

$$\alpha \rightarrow \begin{cases} (\alpha + \alpha)'' \\ (\alpha + \beta)' \\ (\beta + \beta)'' \end{cases} \quad \beta \rightarrow \begin{cases} (\alpha + \alpha)' \\ (\alpha + \beta)'' \\ (\beta + \beta)' \end{cases} \quad (\text{S15})$$

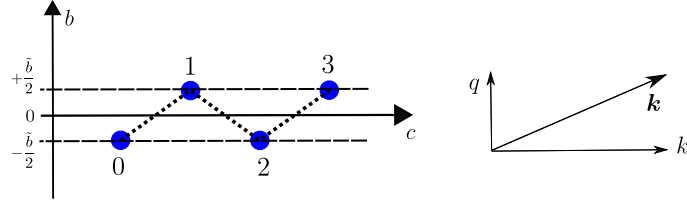


FIG. S2. Geometry of the chain with even/odd sites respectively in position $\mp \tilde{b}/2$.

DSF for off-axis wave-vectors and “shadow mode”

In this section we compute the DSF $\mathcal{S}(\omega, \mathbf{k})$ when the wavevector \mathbf{k} has a non-zero component perpendicular to the c -axis (see Fig. S2): q in the b direction and q' in the a direction, so that $\mathbf{k} = (q', q, k)$. We will show that the DSF can be expressed as a linear combination of the 1d DSF $\mathcal{S}(\omega, k)$ and $\mathcal{S}(\omega, k + \pi/\tilde{c})$ — as well as other 1D terms, that are however small in the case of CoNb_2O_6 . The $\mathcal{S}(\omega, k + \pi/\tilde{c})$ component gives rise to the “shadow mode” discussed in Ref. 14.

The DSF in this more general case is

$$\mathcal{S}^{\alpha\beta}(\omega, \mathbf{k}) \equiv \frac{1}{L} \int_{-\infty}^{\infty} dt \sum_{l,m} e^{i\mathbf{k}(\mathbf{r}_l - \mathbf{r}_m)} e^{i\omega t} \langle S_l^\alpha(t) S_m^\beta \rangle \quad (\text{S16})$$

$$= \frac{1}{L} \int_{-\infty}^{\infty} dt \sum_{l,m} e^{ik(l-m)\tilde{c}} e^{i\omega t} f(l, m) \langle S_l^\alpha(t) S_m^\beta \rangle \quad (\text{S17})$$

with

$$f(l, m) = \begin{cases} e^{iq\tilde{b}} & \text{if } l \text{ is odd and } m \text{ is even,} \\ e^{-iq\tilde{b}} & \text{if } l \text{ is even and } m \text{ is odd,} \\ 1 & \text{otherwise,} \end{cases} \quad (\text{S18})$$

as even(odd) sites have b coordinate of $-\tilde{b}/2$ ($\tilde{b}/2$). Explicitly splitting the sum for even and odd m , and re-expressing sums over l using

$$\sum_l f(l, m)(\dots) = \sum_l \left[f(0, m) \frac{1 + e^{i\pi l}}{2} + f(1, m) \frac{1 - e^{i\pi l}}{2} \right] (\dots) \quad (\text{S19})$$

we obtain

$$\begin{aligned} \mathcal{S}^{\alpha\beta}(\omega, \mathbf{k}) &= \mathcal{S}^{\alpha\beta}(\omega, k) \frac{1 + \cos(q\tilde{b})}{2} + \mathcal{S}^{\alpha\beta}(\omega, k + \pi/\tilde{c}) \frac{1 - \cos(q\tilde{b})}{2} \\ &+ \left[\mathcal{S}_A^{\alpha\beta}(\omega, k) - \mathcal{S}_A^{\alpha\beta}(\omega, k + \pi/\tilde{c}) \right], \sin(q\tilde{b}) \end{aligned} \quad (\text{S20})$$

where we introduced the real function $\mathcal{S}_A^{\alpha\beta} = i(\mathcal{S}_0^{\alpha\beta} - \mathcal{S}_1^{\alpha\beta})$ defined in terms of

$$\mathcal{S}_0^{\alpha\beta}(\omega, \mathbf{k}) \equiv \frac{1}{L} \int_{-\infty}^{\infty} dt \sum_l \sum_{\text{even } m} e^{ik(l-m)\tilde{c}} e^{i\omega t} \langle S_l^\alpha(t) S_m^\beta \rangle \quad (\text{S21})$$

$$\mathcal{S}_1^{\alpha\beta}(\omega, \mathbf{k}) \equiv \frac{1}{L} \int_{-\infty}^{\infty} dt \sum_l \sum_{\text{odd } m} e^{ik(l-m)\tilde{c}} e^{i\omega t} \langle S_l^\alpha(t) S_m^\beta \rangle. \quad (\text{S22})$$

Note that $\mathcal{S}_A^{\alpha\beta}$ would vanish if no staggered term were present. For CoNb_2O_6 , as λ_{yz} is a weak correction to the uniform component of \mathcal{H} , $\mathcal{S}_A^{\alpha\beta}$ will be small.

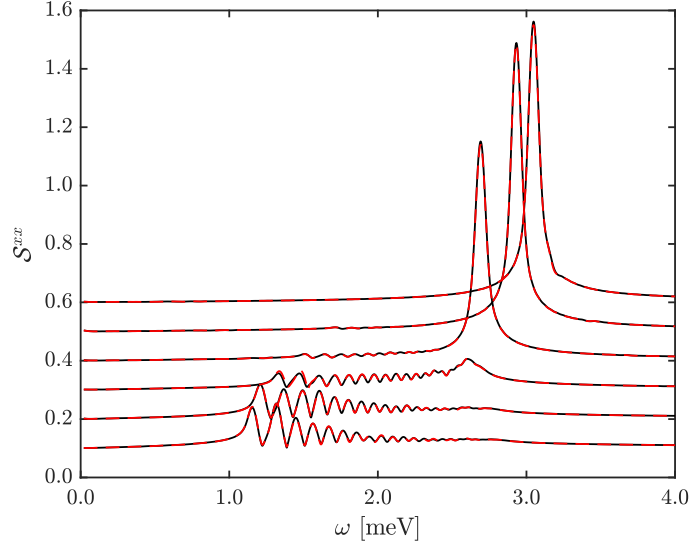


FIG. S3. Convergence analysis for the simulations at $h_y = 0$. The black curve is obtained with tDMRG parameters $\varepsilon = 10^{-10}$ and $\delta t = 5 \cdot 10^{-3}$. Instead, the parameters of the red curve are the same as in Fig. 2. In both cases, $t_{max} = 500/J$ and $\eta = J/125$. The positions of the maxima display a good convergence, especially around $k = 0$ and π/\tilde{c} .

Details of tDMRG computation

Working at $T = 0$, we compute the matrix-product state (MPS) approximation of the ground state $|0\rangle$ of \mathcal{H} on a chain of L sites using DMRG. From this, the state $|\psi\rangle = S_{L/2}^\beta |0\rangle$ can be computed. We then time-evolve the state, viz. $|\psi(t)\rangle = \exp(-iHt)|\psi\rangle$, through tDMRG, up to some maximum time t_{max} . The DSF can then be approximated by [22]

$$S^{\alpha\beta}(\omega, k) = E \left[2\Re \left(\int_0^{t_{max}} dt \sum_i e^{ik(r_i - r_{L/2})} e^{i(\omega + \omega_0)t} \langle 0 | S_i^\alpha | \psi(t) \rangle \mathcal{W}(t) \right) \right]. \quad (\text{S23})$$

Here, we define $E[f](q) = f(q) + f(-q)$, which, exploiting the inversion symmetry about bond centres, is equivalent to averaging over the position of j . Finally $\mathcal{W}(t)$ is a windowing function smoothly suppressing contributions at larger t , in such a way that the truncation at $t = t_{max}$ does not produce oscillations in the Fourier transform (this requires $\mathcal{W}(t_{max}) \ll 1$). In this paper, we use a Gaussian windowing $\mathcal{W}(t) \propto \exp[-(\eta t)^2/2]$ [23]. Due to this choice the DSF obtained from the computation can be viewed as the convolution of the exact DSF with a Gaussian of width η , broadening spectral lines.

There are 3 parameters controlling the errors in the computation:

Trotter step δt : In order to compute the time-evolution we write $\exp(-iHn\delta t) = \exp(-iH\delta t)^n$ and approximate $\exp(-iH\delta t)$ with a 3-local unitary circuit, by employing a second order Trotter decomposition, i.e. the error are $\mathcal{O}(\delta t^2)$.

Singular value cutoff: Both in the DMRG and in the tDMRG, we truncate singular values below a threshold ε .

Hard cutoff on number of singular values: For $h_y \neq 0$ the bond dimension would grow quite rapidly for small enough ε , so we also use an hard-cutoff and keep at most χ singular values at every time.

Exact results are recovered as $\varepsilon \rightarrow 0$ and $\chi \rightarrow \infty$. Fig. S3 we verify the convergence of our simulations for $h_y = 0$, and in Fig. S4 for $B = 2.5$ T. In these cases, we did not employ an hard-cutoff χ since the entanglement growth is very mild.

The convergence analysis for the data in Fig. 3 of the main text is performed in Fig. S5. The larger η used for the simulation in non-zero field are due to the fact that the dynamics in this case produces entanglement more rapidly, therefore t_{max} for $h_y \neq 0$ is shorter than t_{max} at $h_y = 0$.

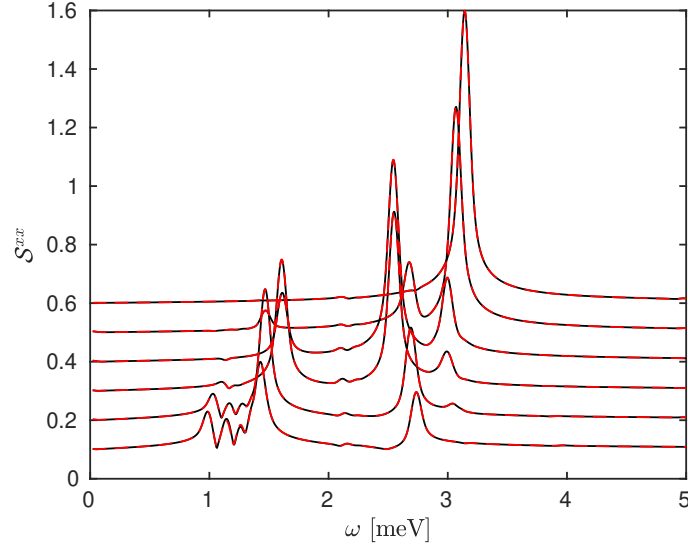


FIG. S4. Convergence analysis for the simulations at $B = 2.5$ T. The black curve is obtained with tDMRG parameters $\varepsilon = 10^{-10}$ and $\delta t = 5 \cdot 10^{-3}$. Instead, the parameters of the red curve are the same as in Fig. 4. In both cases, $t_{max} = 400/J$ and $\eta = J/100$

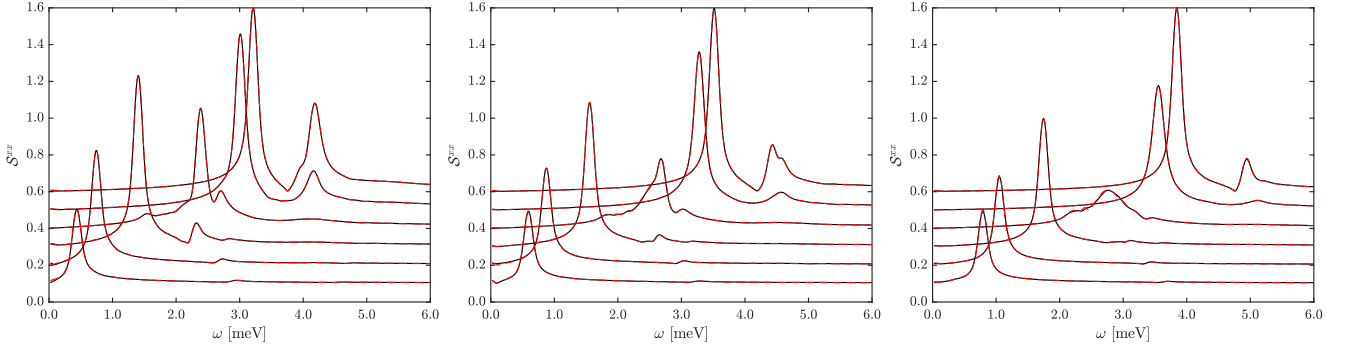


FIG. S5. Convergence analysis for the simulations at (from left to right) $B = 7$ T, 8 T, 9 T. Lines denotes cuts of $\mathcal{S}^{xx}(\omega, k)$ at linearly spaced values of k , going from 0 to π/\tilde{c} . For clarity, as k increases the curves are vertically displaced. The dashed red line is obtained with the tDMRG parameters of Fig. 3; the solid black line, instead, with $\varepsilon = 10^{-9}$, $\chi_{max} = 200$ and $\delta t = 0.01$. In both cases, $t_{max} = 200/J$ and $\eta = J/125$.

Fit of g_b

In order to determine the g -factor g_b , we consider the position of the maxima in the DSF for \mathcal{H} and fit it to the parametrization of the 1QP band at $B = 7$ T reported in [14]. Again, we exploit ED diagonalization on small system sizes. Therefore, to reduce finite-size effects, we consider only the lower part of the band (i.e. the one lying outside the continuum), finding $g_b \simeq 3.100$. Fig. S6 shows the comparison of the tDMRG simulation with the experimental parametrization of the 1QP band.

Unfolding for other Non-Symmorphic Symmetries

The unfolding discussion applies also to other geometries and space groups whenever a non-symmorphic symmetry is a property of the embedding of a low-dimensional layer or chain into 3D space. The possible cases are, apart from the a chain buckling across a glide plane already discussed, (i) a chain twisting around a screw axis and (ii) a layer buckling across a glide plain. Both cases can be dealt as the one treated in the main text, with the only difference of the unitary unfolding transformation U .

For first case, consider an n -fold screw axis, inducing the symmetry transformation $S = T_z \exp(-i2\pi S_j^z/n)$. The

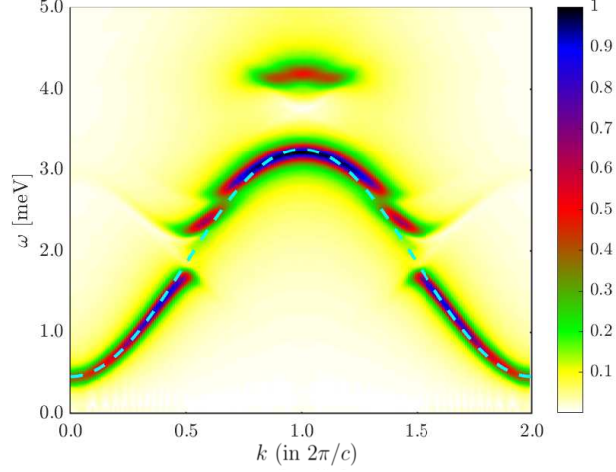


FIG. S6. The colorplot shows $S^{xx}(\omega, k)$ at $B = 7\text{T}$, which is the same as in Fig. 3. The dashed line is the single-particle dispersion relation extracted from fits to the experimental INS data and extrapolated to the case of isolated chains with no interchain couplings [14].

unit cell of the chain will have size $c = n\tilde{c}$. However, taking $U = \otimes_j \exp(i2\pi S_j^z/n)^{m_j}$ with $m_j = j \pmod n$ guarantees that $U^\dagger \mathcal{H} U$ is invariant under $T_{\tilde{c}}$. In this way the BZ probed by the DSF is $2\pi/\tilde{c}$, i.e. n times larger than the “geometric” BZ of size $2\pi/c$.

With regard to case (ii), there are different possibilities given by the geometry of the 2D lattice. Since the unfolding transformation will depend on those, a detailed treatment is beyond the scope of this work.